Spherical magnetic nanoparticles fabricated by laser target evaporation

A. P. Safronov, I. V. Beketov, S. V. Komogortsev, G. V. Kurlyandskaya, A. I. Medvedev, D. V. Leiman, A. Larrañaga, and S. M. Bhagat

COLLECTIONS

Paper published as part of the special topic on Chemical Physics, Energy, Fluids and Plasmas, Materials Science and Mathematical Physics

ARTICLES YOU MAY BE INTERESTED IN
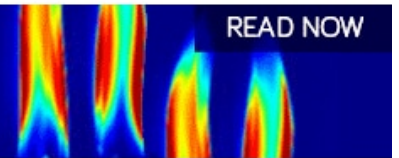
Spherical magnetic nanoparticles fabricated by laser target evaporation

A. P. Safronov,[1,2] I. V. Beketov,[1,2] S. V. Komogortsev,[3]
G. V. Kurlyandskaya,[2,4,a] A. I. Medvedev,[2] D. V. Leiman,[2] A. Larrañaga,[5]
and S. M. Bhagat[6]

[1]*Institute of Electrophysics, RAS, Amundsen St. 106, 620016, Ekaterinburg, Russia*
[2]*Urals Federal University, Lenin St. 51, 620000, Ekaterinburg, Russia*
[3]*Institute of Physics L.V. Kirensky, 660036, Krasnoyarsk, Russia*
[4]*Department of Electricity and Electronics, University of Basque Country UPV-EHU, Box 644, 48080 Bilbao, Spain*
[5]*SGIker, University of Basque Country UPV-EHU, Box 644, 48080 Bilbao, Spain*
[6]*FMR Group, Department of Physics, University of Maryland, 2221 Physics Bldg, College Park, MD 20742, USA*

Magnetic nanoparticles of iron oxide (MNPs) were prepared by the laser target evaporation technique (LTE). The main focus was on the fabrication of de-aggregated spherical maghemite MNPs with a narrow size distribution and enhanced effective magnetization. X-ray diffraction, transmission electron microscopy, magnetization and microwave absorption measurements were comparatively analyzed. The shape of the MNPs (mean diameter of 9 nm) was very close to being spherical. The lattice constant of the crystalline phase was substantially smaller than that of stoichiometric magnetite but larger than the lattice constant of maghemite. High value of M_s up to 300 K was established. The 300 K ferromagnetic resonance signal is a single line located at a field expected from spherical magnetic particles with negligible magnetic anisotropy. The maximum obtained concentration of water based ferrofluid was as high as 10g/l of magnetic material. In order to understand the temperature and field dependence of MNPs magnetization, we invoke the core-shell model. The nanoparticles is said to have a ferrimagnetic core (roughly 70 percent of the caliper size) while the shell consists of surface layers in which the spins are frozen having no long range magnetic order. The core-shell interactions were estimated in frame of random anisotropy model. The obtained assembly of de-aggregated nanoparticles is an example of magnetic nanofluid stable under ambient conditions even without an electrostatic stabilizer. © *2013 Author(s). All article content, except where otherwise noted, is licensed under a Creative Commons Attribution 3.0 Unported License.* [http://dx.doi.org/10.1063/1.4808368]

I. INTRODUCTION

Magnetic nanoparticles (MNPs) of iron oxides have for a long time been the subject of special interest due to properties which are suitable for a large variety of biomedical, environmental and technological applications.[1,2] Although magnetite (Fe_3O_4) is one of the most versatile biocompatible magnetic materials with a high saturation magnetization and a Curie point well above the ambient temperature complemented by a relatively weak magneto-crystalline anisotropy,[3–5] the lack of long term stability of the properties of Fe_3O_4 MNPs encourages researchers to study another iron oxide, maghemite (Fe_2O_3), with focus on particular applications. Despite the disadvantage of a slightly

---

[a]Author to whom correspondence should be addressed. Electronic mail: galina@we.lc.ehu.es.

smaller saturation magnetization in its bulk state[4] Fe_2O_3 offers higher stability and therefore, more predictable response for living systems.

Present day biomedical applications require thorough characterization of MNPs because their properties can vary very much from batch to batch even for well controlled fabrication conditions.[6] Preclinical physicochemical characterization of MNPs includes studies of size, shape, aggregation and/or agglomeration grade etc. for each batch. The last attracts special attention to manufacturing techniques which providing enhanced batch sizes. One such technique is the electric explosion of wire (EEW) which has production rates up to 200 g/h, requires small energy consumption and ensures fabrication of spherical MNPs with an average particle size of 20-100 nm and was discussed in detail recently.[7,8] One of the other techniques employed recently for spherical iron oxide MNPs fabrication is a laser target evaporation method (LTE) which provides slightly lower production rates up to 50 g/h.[7,9] As we shall see it results in the appearance of quite interesting materials, including the possible formation of water-based ferrofluids without using electrostatic stabilizers. Ferrofluids are stable colloidal dispersions of de-aggregated fine particles of a magnetic material, such as magnetite or maghemite, in a liquid, appropriate for specific applications. Magnetic fluids possess the unique combination of fluidity and capability of interacting with external magnetic fields. Biomedical applications demand de-aggregated magnetic MNPs in the form of water-based ferrofluids.

In this work we describe our experiments on preparation, fractionation and extended characterization of ensembles of iron oxide magnetic nanoparticles produced by LTE using different chemical and physical techniques. The main focus was on the fabrication of de-aggregated spherical maghemite MNPs with a narrow size distribution and enhanced effective magnetization, the potential basis for the creation of magnetic nanofluids without electrostatic stabilizers.

II. EXPERIMENTAL PROCEDURE, MATERIALS AND METHODS

A. Method of laser target evaporation

Iron oxide MNPs were prepared by the LTE. The method may be considered as the development of the laser vapor deposition technique.[10,11] Whereas in the case of laser deposition the material is evaporated by a laser beam and then deposited on an appropriate substrate, in the case of LTE the vapors of material are cooled in the gas phase giving rise to condensation of nanoparticles, thereby forming an aerosol. To promote the formation of uniform spherical particles the evaporation is performed in a circulating gas flow, which cools down the vapor and prevents particles from agglomerating. The basics of the LTE approach for production of oxide MNPs are widely described in the literature.[12–14]

For the preparation of LTE MNPs an Ytterbium (Yb) fiber laser with 1.07 μm wavelength was used (Fig. 1). The target α-Fe_2O_3 pellet, 65 mm in diameter and 20 mm in height, was pressed from coarse micron sized powder (specific surface area 0.5–1 m^2/g). Before evaporation the pellet was annealed at 1000ºC for 1 h in air. In the evaporation chamber the target pellet was mounted on a driving mechanism, which provided both rotation and horizontal movement of the pellet. The laser beam was focused onto the target pellet surface by optical system Optoscand d25 f60/200 with 200 mm focal length. The diameter of the focal spot was 0.45 mm. The driving mechanism provided 20 cm/s beam scan rate on the target surface, which ensured uniform wear-out of the target surface. The laser operated in a pulsed regime, favouring the formation of fine uniform MNPs with narrow particle size distribution. The pulse frequency was 5 KHz with pulse duration 60 μs. Average output power of irradiation was about 180 W.

The working gas (a mixture of N_2 and O_2 in the volume ratio 0.79:0.21) was blown into the evaporation chamber by a fan. The gas flow rate was 70 L/min at normal pressure. The linear flow rate at the target surface was approximately 15 m/sec. The oxide vapors were driven away from the focal spot and condensed as spherical MNPs, which were carried by the working gas into the cyclone (Fig. 1) and the fine filter where the powder was collected.
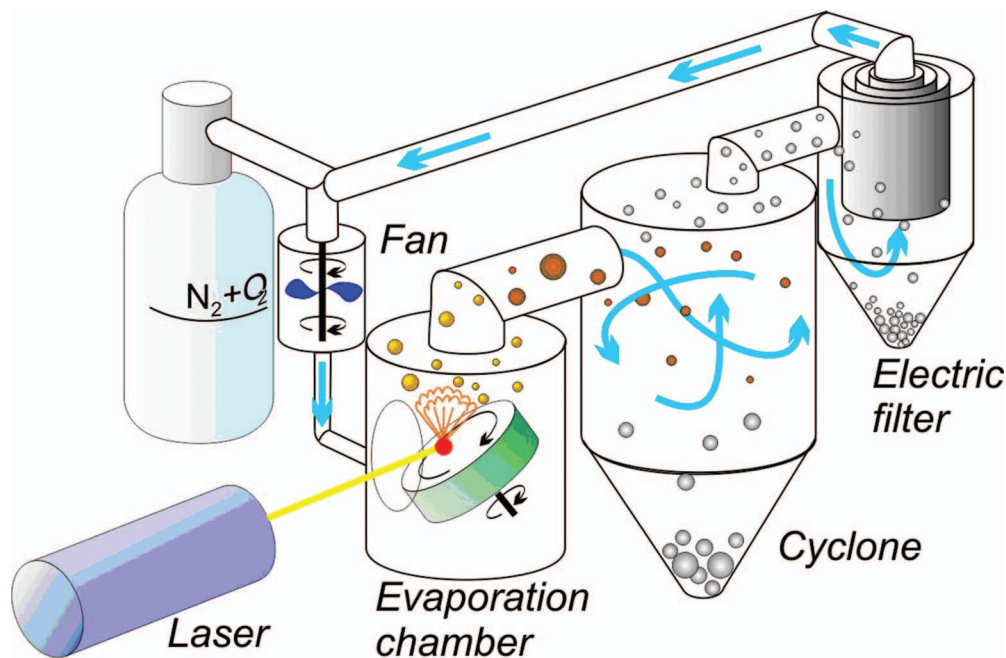
FIG. 1. Schematic diagram of the method of laser target evaporation for fabrication of the iron oxide nanoparticles.

B. Structural characterization methods

The X-ray diffraction (XRD) studies were performed by operating at 40 kV and 40 mA DISCOVER D8 (Bruker) diffractometer using Cu-Kα radiation (λ = 1.5418 Å), a graphite monochromator and a scintillation detector. The MNPs were mounted on a zero background silicon wafer placed in a sample holder. A fixed divergence and antiscattering slit were used. Bruker software TOPAS-3 with Rietveld full-profile refinement was employed for the quantitative analysis of all the diffractograms. The initial Rietveld analysis allowed us to calculate the unit cell parameters, peak shape using the Double-Voigt approach, background, systematic 2θ shift, displacement, and half-width parameters for the profile function. Additionally, the average size of coherent diffraction domains was estimated by using the Scherrer approach.[15]

For transmission electron microscopy (TEM) the particles were spread on carbon-coated copper grids. TEM was performed using a JEOL JEM2100 microscope operating at 200 kV.

The specific surface area (S_{sp}) of MNPs was measured by the low-temperature sorption of nitrogen (Brunauer-Emmett-Teller physical adsorption (BET)) using Micromeritics TriStar3000 analyzer.

The stoichiometric ratio Fe^{2+}/Fe^{3+} in the MNPs was determined by Red-Ox potentiometric titration by potassium dichromate using an automatic titrator TitroLine (Schott Instruments). Titration was performed under an argon atmosphere to prevent oxidation of the Fe^{2+} in the air.

Aggregation of MNPs in water suspension was studied by dynamic light scattering (DLS) using the Brookhaven Zeta Plus particle size analyzer. The electrokinetic zeta-potential of the suspensions was measured by electrophoretic light scattering (ELS) using the same analyzer. All the measurements were made at 298 K in suspensions diluted down to 0.1 g/L by de-ionized water. Ultrasound treatment of the suspensions for the de-aggregation was performed using a Cole-Palmer CPX-750 processor at a 300 W average power output level. Centrifuging of the suspensions was performed using a Hermle Z383 centrifuge with a 218 rotor at a maximum of 15 000 rpm.

De-aggregation of the suspension was performed in the same way as described in our previous reports on iron oxide MNPs produced by the electric explosion of wire (EEW).[8] After exhaustive ultrasound treatment until a constant average hydrodynamic diameter was achieved, the suspension was centrifuged (Hermle Z383) for 5 min at 10 000 rpm. Two types of de-aggregated suspensions were obtained: the first one is a water based suspension without electrostatic stabilizer and the

second one is a water based suspension with Na citrate as an electrostatic stabilizer. Thereafter the samples are designated as follows: as-prepared MNPs – AP; de-aggregated suspension of MNPs suspension without electrostatic stabilizer – DA-I; de-aggregated suspension of MNPs suspension with electrostatic stabilizer DA-II.

C. Magnetic and microwave characterization methods

Magnetic measurements were performed in the temperature range 5 to 300 K by a vibrating sample magnetometer (Cryogenics Ltd. VSM), a superconducting quantum device (Quantum Design MPMS-7) and The Cryogen Free Measurement System (CFMS) from Cryogenic Ltd. We refer to the high field (in a field of 8×10^3 kA/m) value of magnetization as far as the saturation magnetization (M_s) is concerned. Zero-field cooled (ZFC) and field cooled (FC) thermomagnetic curves were measured under an applied magnetic field H = 3.95 kA/m. To obtain ZFC data, the samples were cooled in zero field from room temperature of 300 K down to 5 K, and then the magnetization was recorded with an increasing temperature under the applied constant magnetic field of 3.95 kA/m. For FC data, the process was repeated under the same magnetic field applied both while cooling and heating of the sample.

Very early it become clear that more exotic effects like spin canting or exchange bias should be taken into account during the analysis of the magnetic properties. The first indication of possible presence of such effects is the absence of the saturation well above 800 kA/m. Most likely, disordered surface spins are the cause.[18,19] To further explore possible surface effects an additional set of measurements was specially done as follows: the M (H) loops were obtained at a low temperature of 10 K after cooling in the presence of a magnetic field of 8×10^3 kA/m.

Detailed descriptions of the technique for the microwave studies (ferromagnetic resonance (FMR) and non-resonant zero field absorption) were published in previous works of the FMR Group at The University of Maryland.[4,5,20] It is based on employing a conventional homodyne spectrometer and a half-wavelength rectangular cavity without using field modulation: rather, we measured the microwave absorption (P) itself as a function of the applied magnetic field. The line width of the FMR lines (ΔH) was calculated as the line width at half of the peak intensity. All microwave studies were done at room temperature and 8.85 GHz frequency (f).

The sample preparation procedure for magnetic and microwave studies consisted of mixing MNPs with 7031 GE varnish and evenly spreading the mixture onto a 0.2 mm thick quartz plate. Samples diluted in talc were also prepared for studies of possible effect of intergranular interactions: the MNPs were diluted by mixing them with non-magnetic talc powder and then spread onto the quartz plate with GE varnish.

III. RESULTS AND DISCUSSION

A. Structural characterization

1. Dispersion parameters and de-aggregation

TEM microphotographs and particle size distribution by number of as-prepared LTE iron oxide MNPs are shown in Fig. 2. Particle size distribution is lognormal with median value 9.2 nm and dispersion of 0.368 nm.

The specific surface area of MNPs - 93 m²/g can be used for the evaluation of weighted average diameter (d_w) of spherical MNPs according to the equation:[16,21]

$$d_w = \frac{6}{\rho S_{sp}} \qquad (1)$$

where ρ is the density of MNPs. The obtained value of 14.0 nm is in good agreement with weight average diameter (14.4 nm) calculated using lognormal distribution with aforementioned parameters.

It is known[17] that the MNPs produced by physical condensation in the vapor have a strong tendency to aggregate. By proper choice of LTE parameters it is possible to avoid coalescence of the liquid droplets of the material in the vapor and thus to prevent formation of agglomerates. However, the aggregation of colliding solid particles in the gas phase due to the physical surface forces is
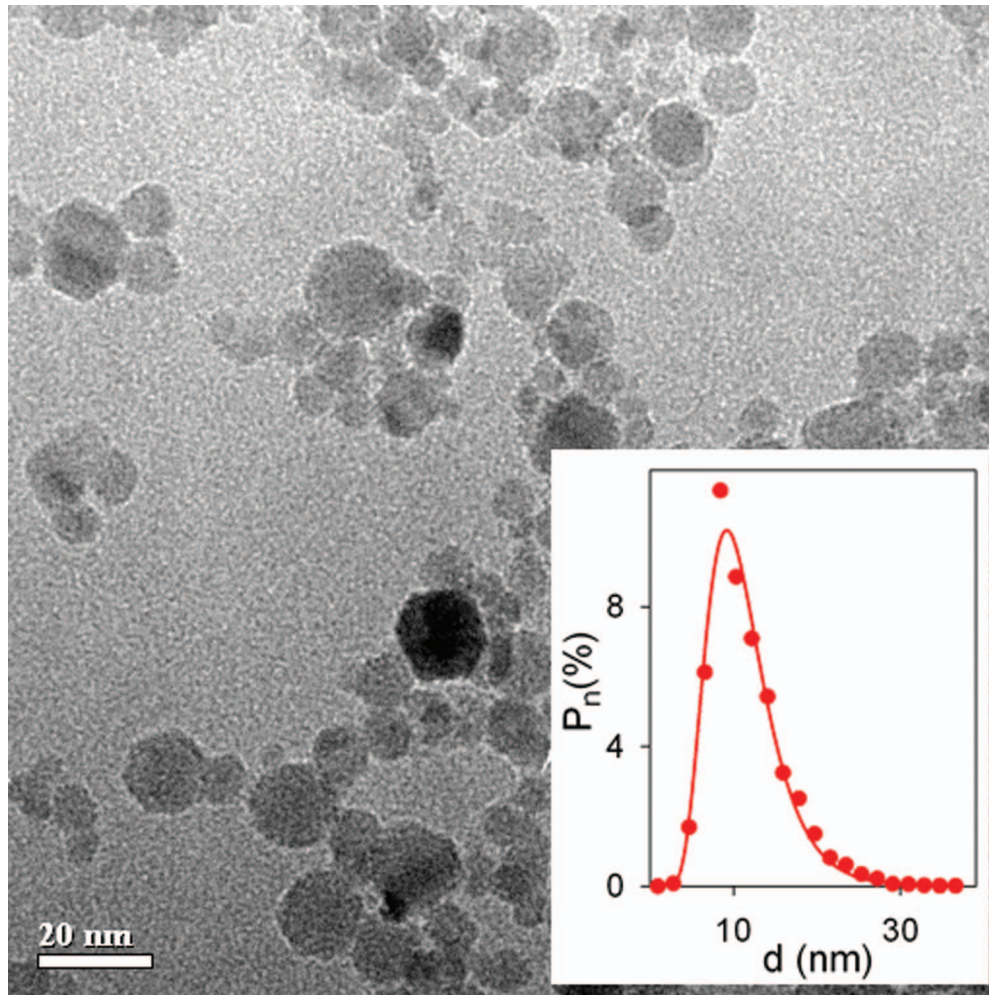
FIG. 2. TEM microphotographs of LTE iron oxide MNPs. Particle size distribution by number was determined by graphic analysis of about 2800 particles.

inevitable. Therefore, iron oxide LTE MNPs contained a fraction of physical aggregates, which was evaluated by means of the dynamic light scattering (DLS) of the water suspension of LTE MNPs.

The necessary condition for the DLS analysis of physical aggregation is the stability of the liquid suspension of MNPs, which is not readily achieved, and in most cases needs the usage of special dispersants. In this respect the important advantage of LTE iron oxide MNPs is their self-stabilization in water suspension. Recently[22] we had reported this feature for the LTE and EEW alumina nanoparticle suspensions, and it had also appeared for LTE iron oxide MNPs.

The air-dry LTE iron oxide can be dispersed in water after an ultrasound treatment of 10 min and can form a stable suspension. The zeta-potential of this suspension determined by electrophoretic light scattering is around +30 mV. The positive value of zeta-potential means that upon the dispersion in water the MNPs become positively charged and repel from each other. According to theoretical considerations and numerous experimental data, the threshold for the colloidal stability of an aqueous suspension is achieved if the absolute value of the zeta-potential exceeds 20 mV irrespective of its sign.[23] The observed positive value of zeta-potential for LTE MNPs suspension was substantially higher providing the effective electrostatic stabilization.

Fig. 3 shows the pH dependence of zeta-potential of water suspension of LTE iron oxide MNPs and the apparent value of the hydrodynamic diameter measured by DLS. At neutral and acidic conditions with pH values within 3 – 7 range the zeta-potential is positive and its absolute values are
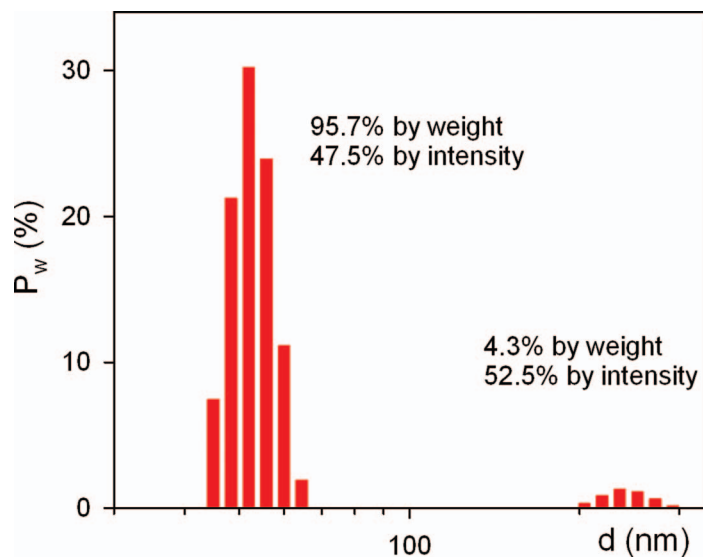
FIG. 3. The pH dependence of zeta-potential (circles) and mean hydrodynamic diameter (squares) in the water suspension of iron oxide MNPs.

substantially higher than the threshold for colloidal stability. The apparent hydrodynamic diameter is around 100 nm almost independent on the pH. If the pH values of the suspension are shifted to the basic conditions, the values of zeta-potential decrease, and tend to change the sign from positive to negative. The zero value of the zeta potential corresponds to pH $\approx$ 7.0. In the nearby pH range 5–9 the absolute values of zeta-potential are lower than the threshold for stability, and the suspension loses its colloidal stability. In this pH region strong aggregation in the suspension takes place, which results in the ten-fold increase of the apparent hydrodynamic diameter. However, in the strong basic media above pH = 10 the apparent hydrodynamic diameter decreases and the colloidal stability of the suspension reappears. The zeta-potential becomes negative, and its absolute value increases to 20 mV.

The origin of high positive values of zeta-potential in the as-prepared suspension of LTE iron oxide MNPs is not readily understood. The pH value of the suspension falls within the interval 4–4.5. It is lower than the pH values of distilled or de-ionized water, which are usually around 6.5 due to the inevitable dissolution of carbon dioxide unless special precautions are taken. Hence, the dispersion of LTE iron oxide MNPs in water shifts the pH value to the slightly acidic conditions. According to Figure 3 such pH values 4–4.5 provide positive values of zeta-potential around +30 mV, which are sufficient for the electrical stabilization of suspension. Peculiarly the low pH values and highly positive zeta-potential were achieved without the addition of any ingredients other than MNPs. As no acid was pre-added to the suspension, we could not attribute the positive values of zeta potential to the adsorption of H+ cations on the MNPs.

In this respect the specific features of self-stabilization of iron oxide MNPs in water are the same as that for the stabilization of EEW alumina published earlier.[22] They stem from the conditions of condensation of nanoparticles in the oxidizing atmosphere ($N_2 + O_2$ mixture) upon laser evaporation. Although nitrogen does not react with oxygen at ambient temperature, the reaction can occur at elevated temperatures in the overheated cloud of atomized vapors of metal oxide giving molecules of nitrogen oxides. The condensed metal oxide nanoparticles can adsorb nitrogen oxides providing the formation of nitrates at their surface. The thermal evolution of nitrogen oxides from the EEW alumina was proved by quadrupole mass-spectrometry.[22] Although the exact chemical composition of the metal nitrates adsorbed at the interface can not be discussed with certainty, it seems reasonable that they can be involved in hydrolytic dissociation in water like any soluble salt of a heavy metal.

Based on these results we may assume the following mechanism of charge formation at the MNPs interface in water suspension. When LTE iron oxide MNPs are dispersed in water, iron nitrates, which are adsorbed at the surface of the particles, dissociate giving free Fe^{z+} cations in the
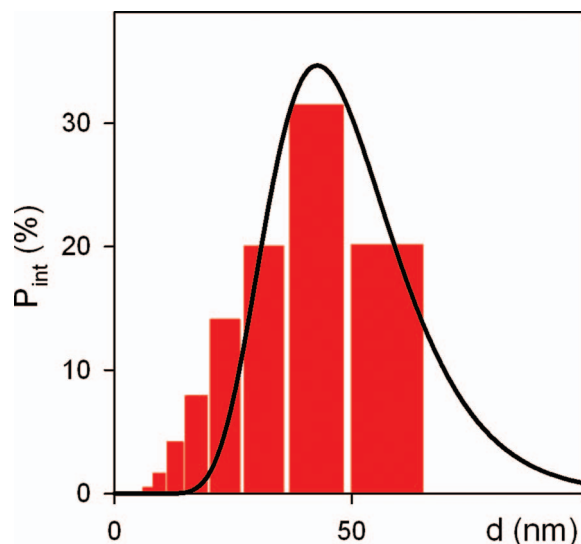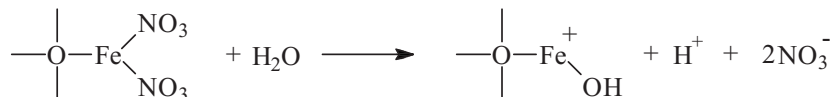
FIG. 4. LTE iron oxide MNPs size distribution by weight in aqueous suspension (DLS, Brookhaven Zeta Plus)

suspension. However, due to the hydrolysis reaction with water molecules, these cations bind with hydroxyl groups providing free H+ cations and the acidic pH in the suspension. Hydrolysed cations (e.g. $FeOH^{(z-1)+}$) adsorb at the MNPs providing positive electric charge at the interface and positive values of zeta-potential. The mechanism is presented step by step for the sake of clarity. Actually it might rather be considered as the hydrolytic dissociation of iron nitrate which is formed chemically bound to the surface.

$$\begin{array}{c} | \\ -O-Fe \\ | \end{array} \begin{array}{c} NO_3 \\ \diagdown \\ NO_3 \end{array} + H_2O \longrightarrow \begin{array}{c} | \\ -O-Fe^+ \\ | \end{array} \begin{array}{c} \\ \diagdown \\ OH \end{array} + H^+ + 2NO_3^-$$

Positive electric charge located on Fe^{z+} cationic sites provides positive charge of the MNPs while nitrate anions act as counterions, which form a double electric layer beneath the surface. Acidic conditions do not affect the structure of the double electric layer. Meanwhile, upon the increase of pH the concentration of hydroxyl anions is enlarged and they adsorb at Fe^{z+} cationic sites. It results in the neutralization of positive surface charge, and in the diminishing of zeta-potential. As the electrostatic stabilization vanishes, the particles aggregate strongly. At high pH values, when all Fe^{z+} cationic sites are already neutralized, the hydroxyl anions adsorb over-equivalently giving rise to the reversal of the sign of the electric charge and zeta-potential from positive to negative. Thus, the electrical stabilization of the suspension is reestablished.

Although the suspension of LTE iron oxide MNPs is stable over a wide range of pH values, the apparent hydrodynamic diameter measured by DLS is much larger than anticipated from the distribution obtained by TEM (Fig. 2). It means that some aggregates are present in the suspension. This fraction can be evaluated by DLS in the multimodal regime.

Fig. 4 shows bimodal particle size distribution by weight obtained by DLS in the stable aqueous suspension of LTE MNPs.

The dominant weight fraction (95.7%) corresponds to the individual MNPs. Although the fraction of aggregates is only 4.3% by weight, its contribution to the intensity of light scattering, which is proportional to the 6-th power of particle diameter, is substantial (52.5%). Therefore, individual MNPs and a small fraction of aggregates scatter light almost equally. As a result, the weight-average particle diameter in the ensemble of individual particles and aggregates determined by DLS was 55 nm. The hydrodynamic diameter, which represents the intensity-average value was substantially higher – 103 nm.

After the separation of aggregates by centrifuging the apparent hydrodynamic diameter measured by DLS decreased substantially to 47 nm. This value is still higher than the average diameter of
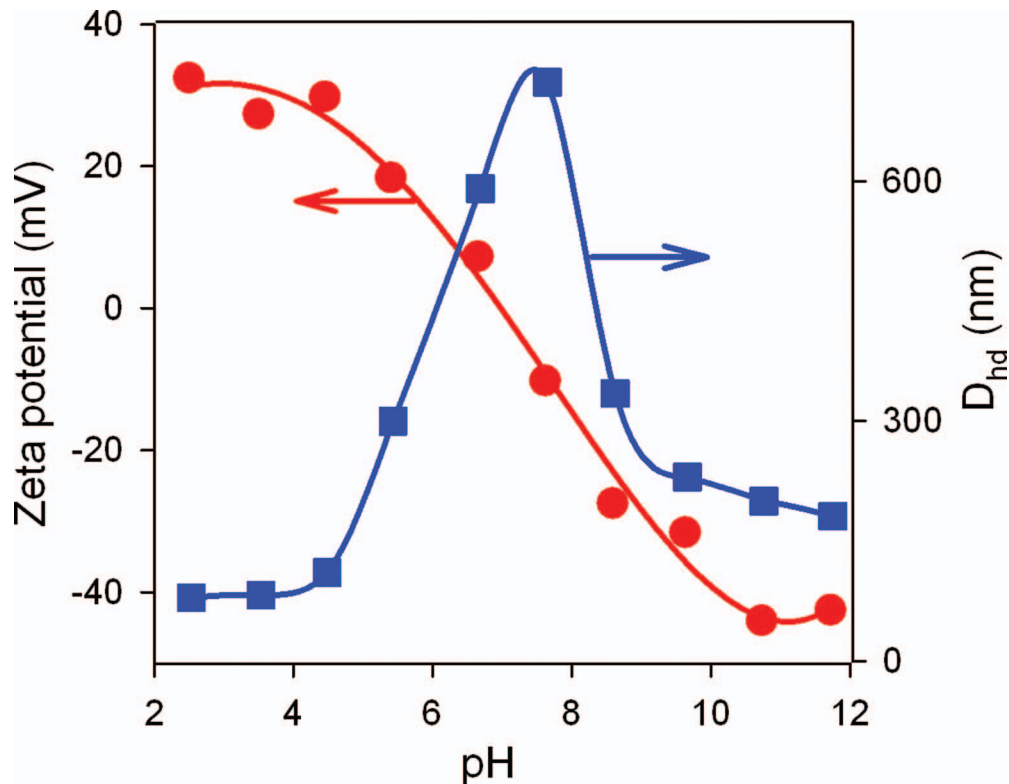
FIG. 5. Particle size distribution of the intensity of light scattering in the suspension of de-aggregated MNPs. Line – determined by DLS. Bars – calculated intensity distribution based on TEM data.

MNPs determined by TEM and calculated using the specific surface area. However, such difference does not indicate aggregation but stems from the high sensitivity of intensity of light scattering to the fraction of large particles in the ensemble of MNPs. Among 2786 particles processed in TEM photograph only 7 were larger than 40 nm. It made their contribution to the number and weight average diameter negligible. The intensity average (hydrodynamic) diameter calculated for this ensemble is 39 nm, which is fairly close to the value of hydrodynamic diameter measured by DLS. The MNPs size distribution by intensity obtained by DLS of de-aggregated suspension fitted well the size distribution by intensity calculated from TEM data (Fig. 5). Thus we conclude that the suspension contained mostly single LTE iron oxide MNPs.

2. Crystalline structure

Fig. 6 shows XRD plots of the as-prepared and de-aggregated LTE MNPs. The experimental points are fitted well by the magnetite XRD database. However, it is well known that the magnetite (Fe_3O_4) structure can not be distinguished from that of maghemite (γ-Fe_2O_3) based only on XRD data.[24] The crystalline cells of both oxides correspond to the inverse spinel structure with space group Fd3m.[25] The spinel elementary cell consists of 32 anions O^{2-} densely packed in a cubic lattice. The Fe^{z+} cations are located between the anions in two sublattices, which differ in coordination number. The "A" sublattice is formed by 8 tetrahedral cation sites, while the "B" sublattice consists of 16 octahedral cation sites.

In the case of magnetite (Fe_3O_4) both cation sublattices are fully occupied by Fe cations: the sublattice A contains eight Fe^{3+} ions, and the sublattice B – eight Fe^{3+} and eight Fe^{2+} ions. Thus, the chemical composition of the cell may be written as $(Fe^{3+}_8)_A[Fe^{3+}_8Fe^{2+}_8]_BO_{32}$. The exact positions of Fe^{3+} and Fe^{2+} cations in the B sublattice can not be specified as there is the spontaneous exchange of electrons between them.[26]
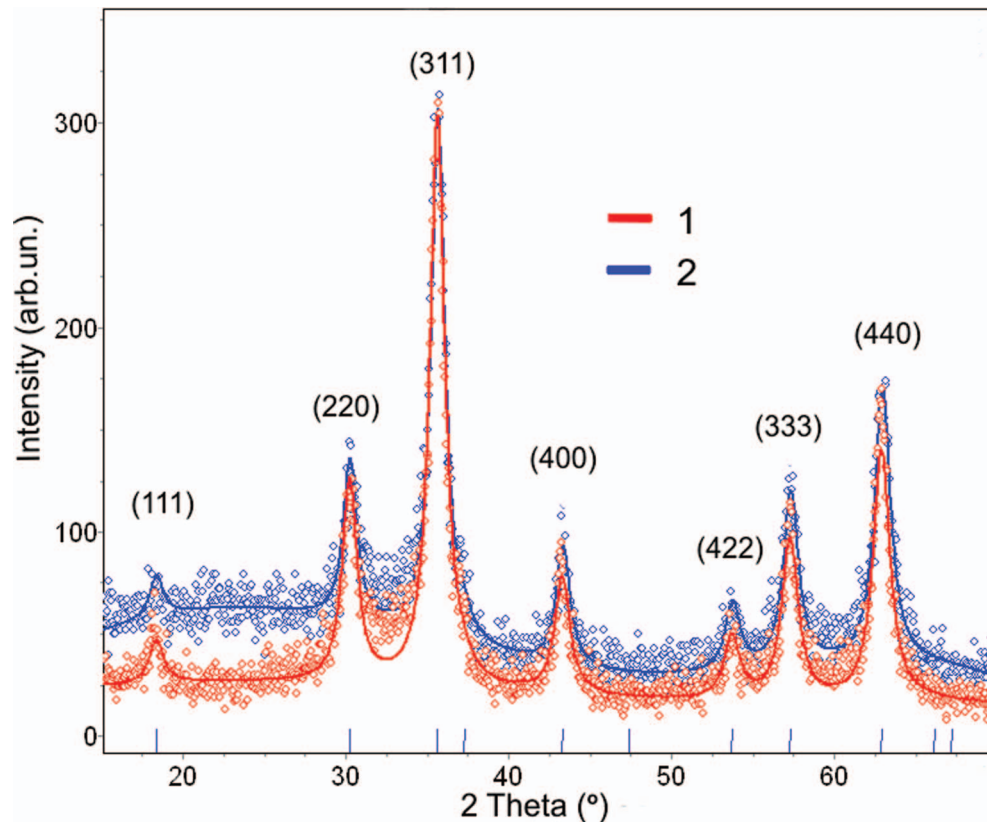
FIG. 6. XRD plots of as-prepared (1) and de-aggregated (2) LTE iron oxide MNPs. Points – experimental diffraction values, line – fitting by the database magnetite structure.

Maghemite (γ-Fe_2O_3) crystalline structure is basically the same, despite the fact that several cation sites in the B sublattice remain vacant. Thus, the Fe/O ratio in the elementary cell decreases and therefore the effective state of oxidation for Fe cations increases. Stoichiometric γ-Fe_2O_3 composition obtains if octahedral sites in the B sublattice are occupied only by Fe^{3+} cations. However, due to the electroneutrality condition several cation sites in B sublattice should remain vacant. Simple calculation gives the chemical composition $(Fe^{3+}_8)_A[Fe^{3+}_{13.33}Fe^{2+}_{2.66}]_B O_{32}$ for the maghemite cell, with Fe^{2+} standing for the cation vacancies in the B sublattice. Thus, from 2 to 3 cation octahedral sites in the elementary cells of the spinel structure of γ-Fe_2O_3 remain vacant. In some cases these vacancies can be ordered, providing extra peaks in XRD plots, but in general there is no ordering of vacancies.

The chemical composition of LTE MNPs was determined by the combination of Red-Ox titration and the analysis of the spinel lattice period provided by XRD.

The non-stoichiometry of LTE iron oxide with regard to magnetite was calculated from the titrated amount of Fe^{2+} and the total amount of Fe in MNPs. The chemical composition of MNPs found by Red-Ox titration was $Fe_{2.68}O_4$ which was very close to the stoichiometric maghemite γ-$Fe_2O_3(Fe_{2.67}O_4)$.

The analysis of the XRD parameters was based on the relationship between the lattice period of spinel cell and the effective state of oxidation of Fe.[27] Although the crystalline structures of magnetite and maghemite are basically the same, the Fe^{3+} cations are slightly smaller than Fe^{2+} cations, and, hence, the lattice constant of maghemite[23] (8.346 nm) is a little bit lower than that of magnetite[23] (8.396 nm). The XRD parameters for LTE MNPs given in Table I show that the lattice constants of the crystalline phase both for as-prepared and de-aggregated MNPs are substantially lower as compared to that of stoichiometric magnetite Fe_3O_4 but higher than the lattice constant of maghemite γ-Fe_2O_3. The obtained lattice constant in LTE MNPs (Table I) gives the effective state

TABLE I. XRD parameters of LTE iron oxide MNPs.

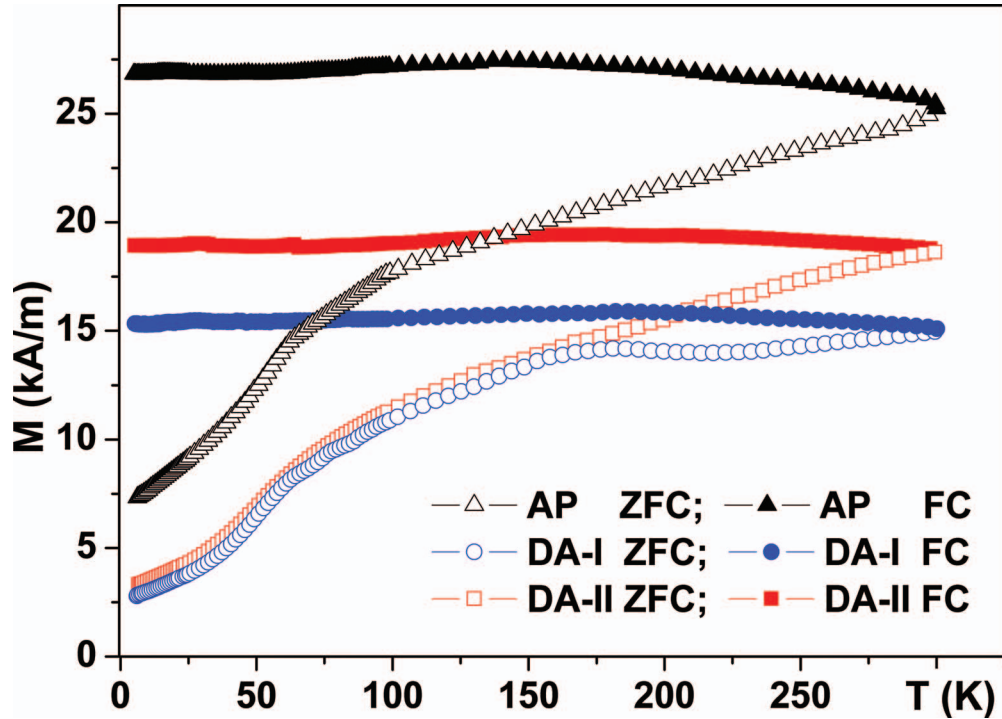| Sample	Lattice period, nm	Average size of crystallites, nm
As-prepared MNPs	0.8354 ± 0.0005	9.3 ± 0.3
De-aggregated MNPs	0.8353 ± 0.0005	9.1 ± 0.3

FIG. 7. ZFC-FC curves measured with 3.95 kA/m for the investigated samples.

of oxidation as +2.918 for Fe cations. It corresponds to the chemical composition $Fe_{2.73}O_4$ for LTE MNPs, which is fairly close to that determined by Ox-Red titration.

Thus, based on XRD and chemical analysis we concluded that LTE MNPs have inverse spinel structure with the composition of the elementary cell $(Fe^{3+}_8)_A[Fe^{3+}_{13.67}Fe^{2+}_{2.33}]_BO_{32}$, which is very close to maghemite but contained slightly fewer number of cation vacancies per cell.

The average sizes of crystallites both for as-prepared and de-aggregated LTE MNPs are almost the same (Table I) and they are very close to the median value of particle size distribution obtained by TEM (9.2 nm). It means that the individual MNPs are essentially mono crystalline. As the de-aggregation did not affect the average size of crystallites, we assume physically bonded aggregates, which were separated during centrifuging consisted of the same mono crystalline MNPs. Maximum obtained concentration of water based ferrofluid was as high as 10g/l of magnetic material.

B. Magnetic and microwave characterization

1. Magnetic characterization

In Figs. 7 through 10 are collected together the results of the measurements of magnetization (M) as a function of temperature (T) and applied field (H). The following points are worthy of note:

1.   The FC and ZFC curves of Fig. 7 show no evidence of a transition from a superparamagnetic (SPM) to a blocked (BL) state. As we shall see this leads us to propose that at 300K the BL
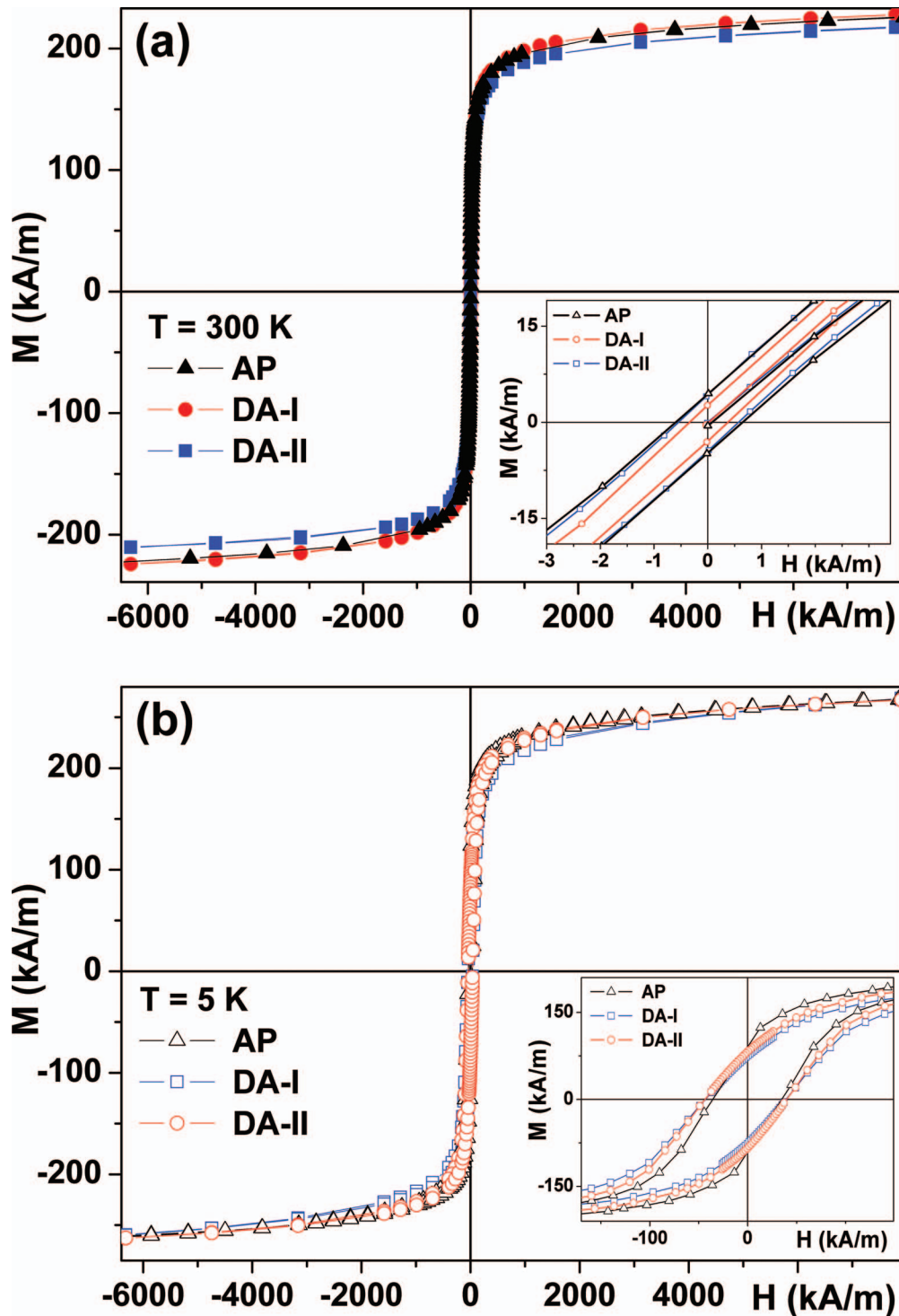
FIG. 8. Magnetization curves measured at T = 5 K and 300 K for the investigated samples.

state prevails. The DA-I and DA-II magnetization values are nearly equal which suggests that inter particle interactions[11] are not important.

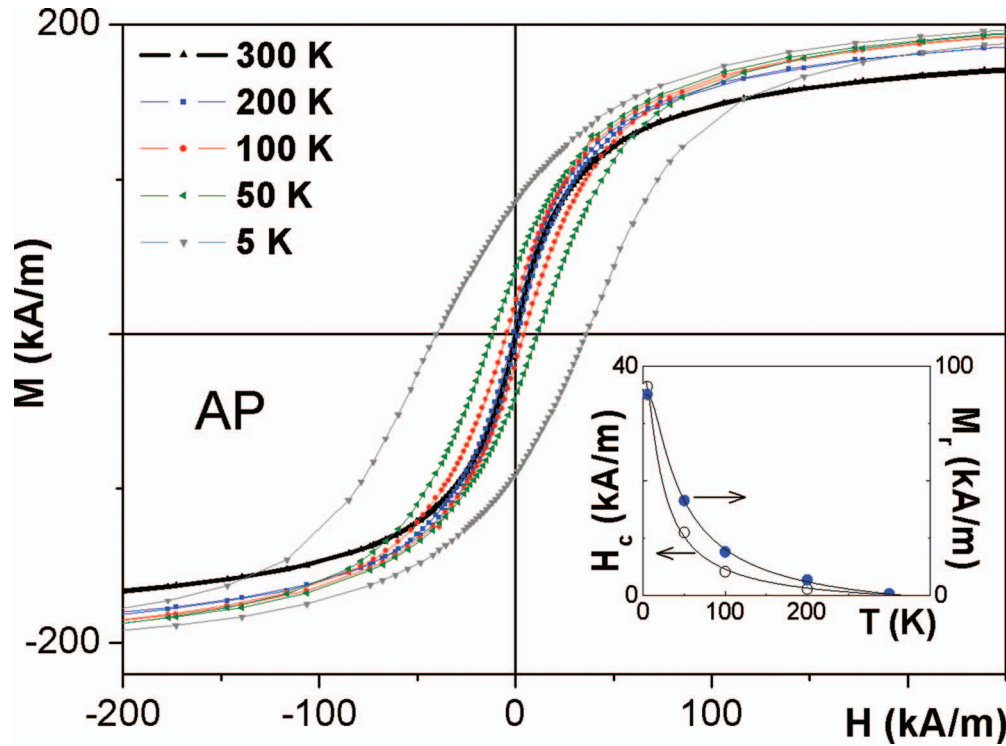2. There is no significant difference between the shapes of the M vs H curves at 300 K and 5 K (Fig. 8).

FIG. 9. Hysteresis loops for the AP sample. The inset - $M_r(T)$ and $H_c(T)$: solid lines show following dependencies: $M_r = 87.6 - 98.7 \times e^{-38/T}$ and $H_c = 37.5 - 39.8 \times e^{-19/T}$ (both in kA/m).

3. Hysteresis loops (Fig. 9) also have similar shapes with coercive fields changing from about 3.95 kA/m at 5 K to 160 A/m at 300 K.
4. Fig. 9 shows further details of the effects of temperature on hysteresis in AP sample. The inset gives the remanence $M_r = 87.6 - 98.7 \times e^{-38/T}$ and $H_c = 37.5 - 39.8 \times e^{-19/T}$ (both in kA/m). In both cases the drop is much sharper than the power laws expected from transition to the SPM phase.[28–31]
5. Figs. 10(a) and 10(b) show the approach to "saturation" at high fields of 0.24 MA/m to 8 MA/m for AP and DA particles respectively. In both cases the nonzero high field susceptibility is evident.

Fig. 11 shows schematically the model we are invoking in order to understand the magnetic behaviour. At the outset it should be noted that no inter particle coupling is included. Each MNP grain is taken to consist of two parts:

(i)   a ferri-magnetic maghemite core with an anisotropy field of about 20 kA/m;
(ii) a surface shell of thickness delta (Δ) in which the spins are frozen but there is no long range magnetic order yielding a "spin glass" like state.

The complexity of the magnetic response is to be attributed to the large random exchange fields, and the concomitant anisotropy, experienced by the core due to the coupling to the "surface" spins. Recall that no inter particle coupling is invoked. Rather, each grain is treated as a complete system.

As mentioned above the ZFC-FC curves of Fig. 7 suggest that MNPs are blocked at 300 K. If K is the energy density required to orient the entire grain ("core + shell") moment and V is the volume we need $KV > 25\,kT$. Since V is small (d = 9 nm) this implies $K = 2 \times 10^5$ J/m^3 which is much larger than the anisotropy energy density for bulk maghemite[32] (5×10^3 J/m^3). Most likely this arises from the coupling between the frozen surface spins and the relatively free core moments (Table II below).
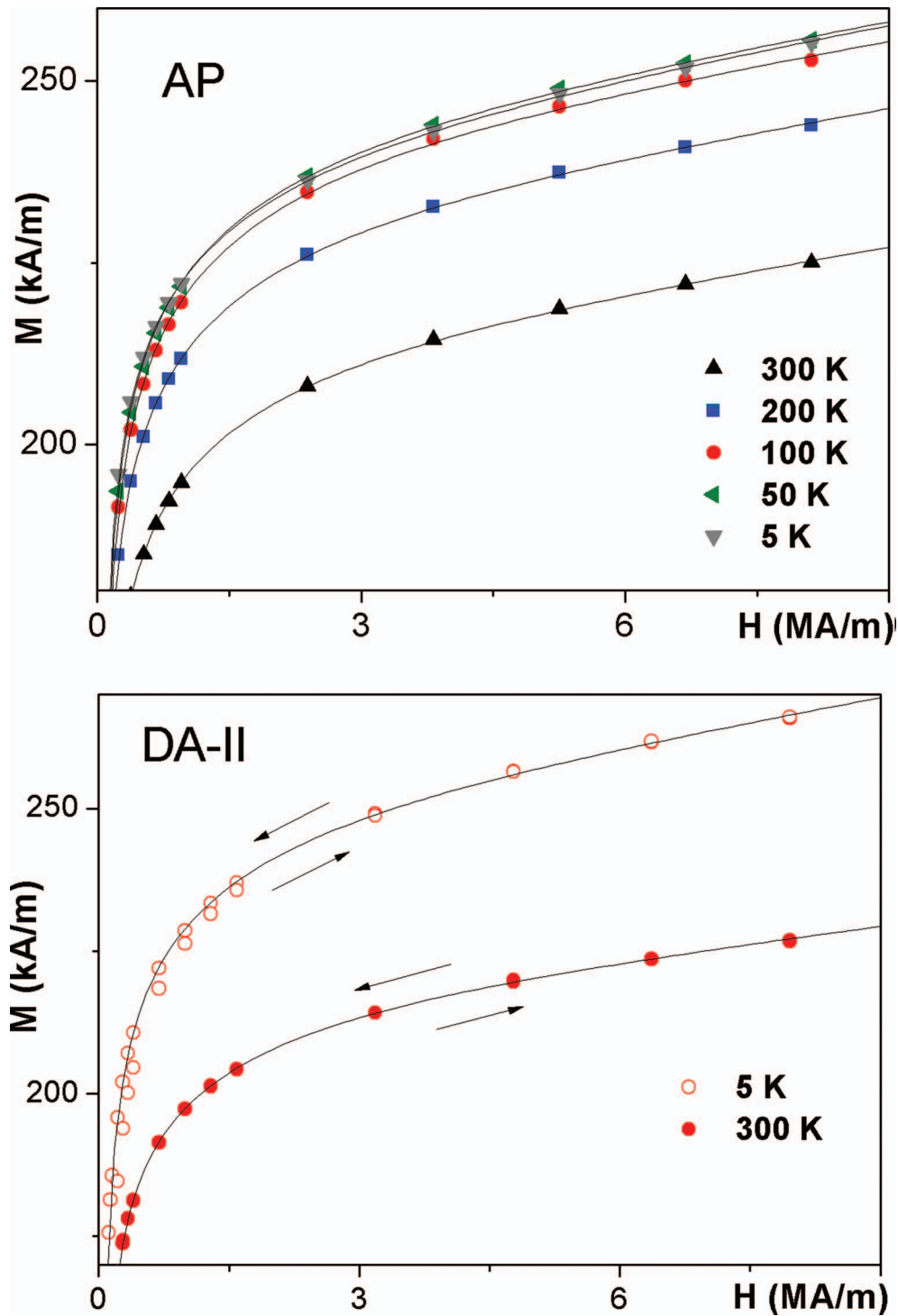
FIG. 10. Approach to magnetic saturation curves at 5 K and 300 K for the samples AP and DA-II. Solid lines – fitting by equation (2).

The current model also receives confirmation from the observation (graphs are not shown here) that hysteresis persists up to applied fields of 4 MA/m at 5 K and cooling in a field of 8 MA/m causes a shift in the loop.

The most telling support for the "core-shell" model comes from looking at the H dependence of M at high fields, i.e., approach to saturation. Several papers have invoked the exchange field (H_r)

TABLE II. Magnetic parameters of maghemite nanoparticles at temperature 5 and 300 K. Errors for H_a and H_R are $\pm$ 0.16 MA/m, for M_s is $\pm$ 10 kA/m, for χ is $\pm$ 2 · 10^{-4}.

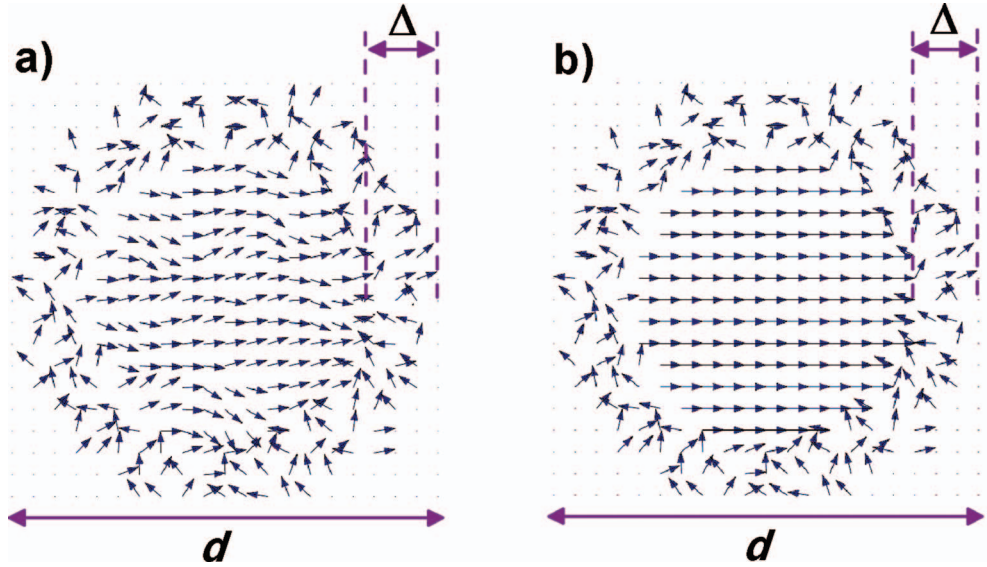| T	5 K				300 K			
sample	H_a, MA/m	H_R, MA/m	M_s, kA/m	χ, 10^{-3}	H_a, MA/m	H_R, MA/m	M_s, kA/m	χ, 10^{-3}
AP	2.6	2.9	249	2.2	2.6	2.7	210	1.9
DA-I	3.3	3.5	244	3.1	3.0	3.1	`205	1.3
DA-II	3.2	3.5	249	2.0	3.2	3.5	215	1.3

FIG. 11. The schematic core-shell structure of iron oxide nanoparticle: (a) – in the medium fields ($\sim$80 kA/m); (b) – in the high fields ($\sim$800 kA/m).

and the anisotropy field (H_a) to write[33–35]

$$M(H) = M_s \cdot \left(1 - \frac{1}{15} \cdot \frac{H_a^2}{H^{1/2} \cdot (H^{3/2} + H_R^{3/2})}\right) + \chi \cdot H \tag{2}$$

where χH represents the weak response of the shell.[19] The full lines in Fig. 10(b) were obtained from this equation with saturation M_s, H_r and H_a values listed in Table II.

First, we note that $H_r \approx H_a$ indicating a common origin for these terms as arising from the interaction of the disordered shell spins with those in the core. The next step is to try and obtain an estimate for the shell thickness delta. It is contended that M_s for MNPs is less than the bulk value due to lack of contribution form the shell spins. If so, for spherical particles of diameter d one can write

$$M = M_{bulk}(1 - 2\Delta/d)^3 \tag{3}$$

and the relevant values are listed in Table III. Presumably, the larger value of delta in magnetite[4, 8, 36] than that in maghemite nanoparticles[37–41] causes the inversion shown in Fig. 12 for large d values.

It is also instructive to look at the temperature dependence of M_s. For bulk ferromagnets one has the well known formula[42]

$$M_s(T) = M_s(0) \cdot (1 - B \cdot T^\alpha) \tag{4}$$

with $\alpha = 3/2$ for thermal magnons in the bulk ferro or ferrimagnet. As shown in Fig. 13 for the AP particles $\alpha = 2.3$ consistent with previous findings.[42–46] This is to be expected because the finite size of the NP does not allow for long wavelength spin waves.[42]
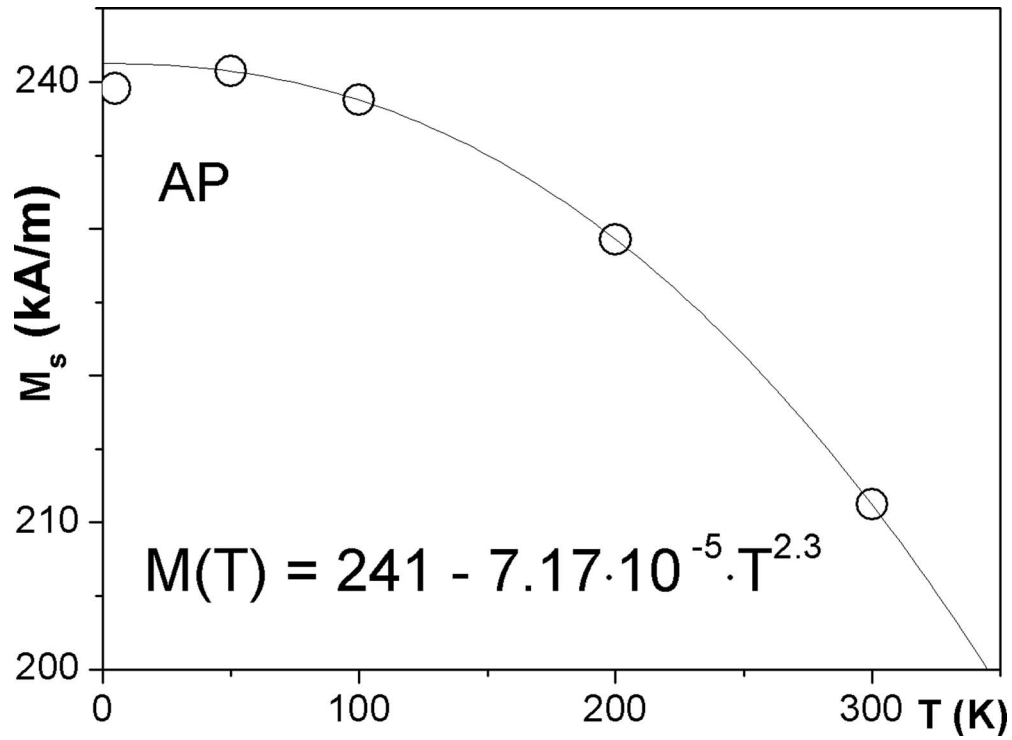
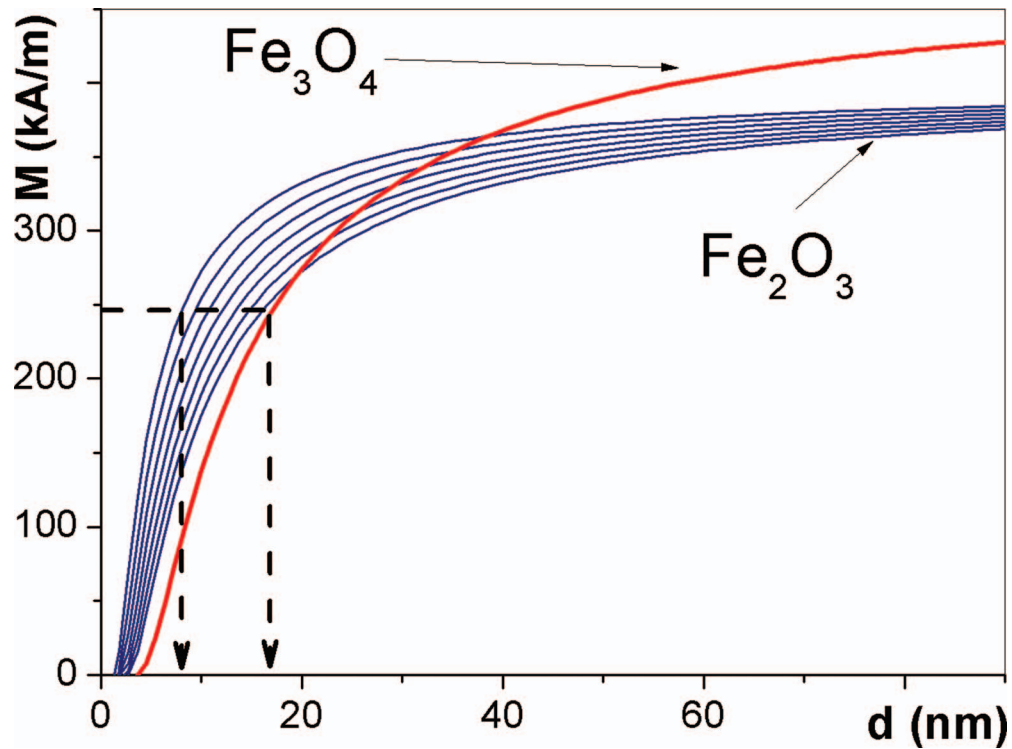FIG. 12. M(T) dependence for AP sample. The solid line fitting by $M_s(T) = M_s(0) \cdot (1 - B \cdot T^\alpha)$.

FIG. 13. The particle size dependences of the magnetization for magnetite and maghemite according to Eq. (3). The literature data for the $\triangle$ magnetite,[4,8,36–41] and the magnetizations of bulk magnetite[32] 480 kA/m and maghemite[32] 400 kA/m are used. Dashed arrows indicate the estimate of the maghemite particles size from saturation magnetization ($\sim$ 250 kA/m).

TABLE III. Magnetization of magnetite and maghemite nanoparticles at temperature 300 K (diameter d = 9 nm, Δ - surface shell of thickness).

Sample	M_s (bulk), kA/m	M_s (MNP), kA/m	Δ, nm
Magnetite	480	120	1.7
Maghemite	400	260-190	0.6-1.2

2. Macrowave characterization

The he microwave absorption was studied in all of the current samples of MNPs at 300 K and 8.85 GHz. It is amazing that all of the complexity noted above arising from the frozen spins in the shell has little or no effect on the field location of the resonance. Rather, the resonance occurs at resonance field $H_{res} = 3.05 \pm 0.1$ kOe as would be expected for a spherical sample of a ferromagnet with a g-value of 2.1 (which is quite reasonable for magnetite) and a negligible anisotropy.[5,47]

$$\frac{\omega}{\gamma} = H_{res} \tag{5}$$

where $\omega = 2\pi f$ is the microwave frequency and γ is the gyromagnetic ratio: $\gamma = 1.1 \times 10^5 g(\frac{m \times mradns}{A})$.

Fig. 14 shows the effect of dilution with talc and again we note no shift which clearly shows that inter-granular coupling if any is negligible. The line widths are about 1 kOe and this may be partly due to distribution of internal fields but it must be noted that mono-crystalline magnetite films also exhibit wide lines. The simplest way to understand the microwave response is to claim that at
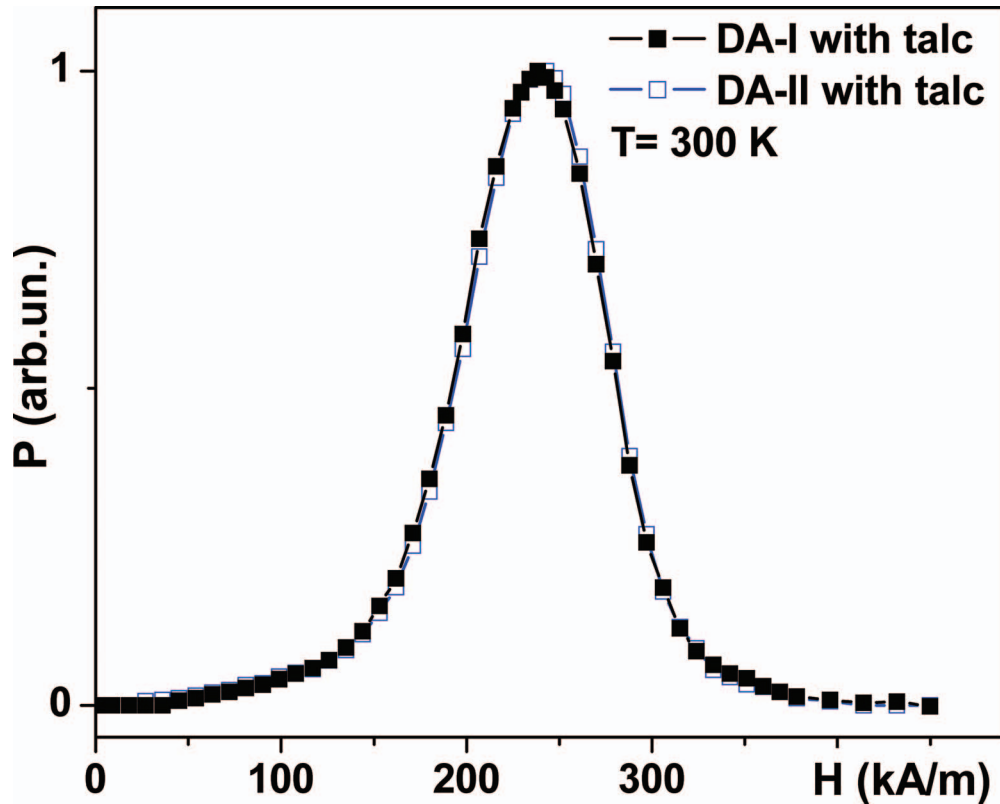

FIG. 14. Microwave losses at f = 8.85 GHz as a function of the external magnetic field. MNPs produced by LTE: DA-I sample after separation and without electrostatic stabilizer, DA-II sample after separation and with electrostatic stabilizer both diluted by talc.

these low fields only the relatively free spins in the core (Fig. 11(a)) participate. In a way this is consistent with the observation that in spite of the very complex approach to saturation the coercive field is rather small.

IV. CONCLUSIONS

We described our experiments on preparation, fractionation and characterization of ensembles of iron oxide magnetic nanoparticles produced by laser target evaporation method using different chemical and physical techniques. The shape of the MNPs was very close to being spherical and the particle size distribution was lognormal with mean diameter value of about 9 nm. The specific surface area of MNPs was as high as 93 m^2/g. The lattice period of the crystalline phase was lower as compared to that of magnetite but higher than the lattice period of maghemite. High values of M_s up to 300 K encourage prospects of LTE MNPs as the magnetoactive component for ferrofluids. The value of M_s in spherical LTE MNPs is considerably larger than that in EEW MNPs of the same size ($\sim$9 nm). Observed magnetic behavior was described in terms of core-shell structure of individual nanoparticle taking into account the effect of the interaction of the core magnetization and the shell of the particle. Maximum obtained concentration of water based ferrofluid stable in the ambient conditions without electrostatic stabilizer was as high as 10g/l of magnetic material. It is interesting magnetic material for technological and biomedical applications.

ACKNOWLEDGMENTS

[1] Y.-W. Jun, J.-W. Seo, and J. Cheon, Acc. Chem. Res. **41**, 179 (2008).
[2] Q. A. Pankhurst, J. Connolly, S. K. Jones, and J. Dobson, J. Phys. D: Appl. Phys. **36**, R167 (2003).
[3] R. C. O´Handley, *Modern Magnetic Materials* (John Wiley & Sons, New York, 1972) p. 740.
[4] G. V. Kurlyandskaya, S. M. Bhagat, A. P. Safronov, I. V. Beketov, and A. Larrañaga, AIP Advances **1**, 042122 (2011).
[5] G. V. Kurlyandskaya, J. Cunanan, S. M. Bhagat, J. C. Aphesteguy, and S. E. Jacobo, J. Phys. Chem. Sol. **68**, 1527 (2007).
[6] J. H. Grossman and S. E. McNeil, Physics Today, 38 (August, 2012).
[7] Yu. A. Kotov, J. Nanoparticle Res. **5**, 539 (2003).
[8] I. V. Beketov, A. P. Safronov, A. I. Medvedev, J. Alonso, G. V. Kurlyandskaya, and S. M. Bhagat, AIP Advances **2**, 022154 (2012).
[9] V. V. Osipov, V. V. Platonov, M. A. Uimin, and A. V. Podkin, Technical Phys. **57**, 543 (2012).
[10] J. M. Barandiaran, P. Minguez, and G. V. Kurlyandskaya, J. Non-Cryst. Solids **239**, 8 (2003).
[11] L. Lanotte, G. Ausanio, A. C. Barone, C. Hison, V. Iannotti, S. Amoruso, R. Bruzzese, M. Vitiello, M. D'Incau, and P. Scardi, J. Optoel. Adv. Mater. **8**, 1672 (2006).
[12] E. Muller, Ch. Oestreich, U. Popp, G. Michel, G. Staupendahl, and K.-H. Henneberg, J. KONA-Powder and Particle **13**, 791 (995).
[13] H.-D. Kurland, J. Grabow, G. Staupendahl, W. Andra, S. Dutz, and M. E. Bellemann, J. Magn. and Magn. Mater. **311**, 73 (2007).
[14] H.-D. Kurland, J. Grabow, G. Staupendahl, F. A. Muller, E. Muller, W. Andra, S. Dutz, and M. E. Bellemann, J. Magn. Magn. Mater. **321**, 1381 (2009).
[15] P. Scherrer, Nachr Ges Wiss Göttingen **26**, 98 (1918).
[16] P. C. Hiemenz, *R. Rajagopalan Principles of Colloid and Surface Chemistry* (Marcel Dekker, New York, 1997), p. 648.
[17] Y. Zhang, Y. Chen, P. Westerhoff, K. Hristovski, and J. C. Crittenden, Water Res. **42**, 2204 (2008).
[18] J. Lee, T. Isobe, and M. Senna, J. Colloid Interface Sci. **177**, 490 (1996).
[19] R. H. Kodama, A. E. Berkowitz, E. J. McNiff, and S. Foner, Phys. Rev. Lett. **77**, 394 (1996).
[20] V. V. Srinivasu, S. E. Lofland, S. M. Bhagat, K. Ghosh, and S. D. Tyagi, J. Appl. Phys. **86**, 1067 (1999).
[21] P. Galletto, W. Lin, and M. Borkovec, Phys. Chem. Chem. Phys. **7**, 1464 (2005).
[22] A. P. Safronov, E. G. Kalinina, T. A. Smirnova, D. V. Leiman, and A. V. Bagazeev, Rus. J Phys. Chem. A **84**, 2122 (2010).
[23] M. Kosmulski, *Chemical properties of material surfaces* (Marcel Dekker, New York, Basel, 2001) p. 248.
[24] I. S. Lyubutin, C. R. Lin, Yu. V. Korzhetskiy, T. V. Dmitrieva, and R. K. Chiang, J. Appl. Phys. **106**, 034311 (2009);
[25] J. B. Goodenough, *Magnetism and the Chemical Bond* (Interscience, New York, 1963), p. 160.
[26] S. Brice-Profeta, M.-A. Arrio, E. Tronc, N. Menguy, I. Letard, C. Cartier dit Moulin, C. Nogues, C. Chaneac, J.-P. Jolivet, and Ph. Sainctavit, J. Magn. Magn. Mater. **288**, 354 (2005).

[27] W. B. Pearson, *Handbook of lattice spacing structures of metals and alloys* (Pergamon Press, London, 1958) p. 1044.

[28] L. Neel, Ann. Geophysique **5**, 99 (1949).

[29] H. Pfeiffer, Phys. Stat. Sol. (a) **120**, 233 (1990).

[30] M. P. Sharrock, J. Appl. Phys. **76**, 6413 (1994).

[31] S. V. Komogortsev, R. S. Iskhakov, A. D. Balaev, A. G. Kudashov, A. V. Okotrub, and S. I. Smirnov, Phys. Solid State **49**, 734 (2007).

[32] J. M. D. Coey, *Magnetism and Magnetic Materials* (Cambridge University Press, New York, 2010) p. 628.

[33] V. A. Ignatchenko, R. S. Iskhakov, and G. V. Popov, Sov. Phys. JETP **55**, 878 (1982).

[34] E. M. Chudnovsky, W. M. Saslow, and R. A. Serota, Phys. Rev. B **33**, 251 (1986).

[35] R. S. Iskhakov and S. V. Komogortsev, Phys. Met. Metallogr. **112**, 666 (2011).

[36] T. Kim and M. Shima, J. Appl. Phys. **101**, 09M516 (2007).

[37] H. M. Lu, W. T. Zheng, and Q. Jiang, J. Phys. D: Appl. Phys. **40**, 320 (2007).

[38] A. Millan, A. Urtizberea, N. J. O. Silva, F. Palacio, V. S. Amaral, E. Snoeck, and V. Serin, J. Magn. Magn. Mater. **312**, L5 (2007).

[39] T. N Shendruk, R. D. Desautels, B. W. Southern, and J. van Lierop, Nanotechnology **18**, 455704 (2007).

[40] E. L. Verde, G. T. Landi, M. S. Carriao, A. L. Drummond, J. A. Gomes, E. D. Vieira, M. H. Sousa, and A. F. Bakuzis, AIP Advances **2**, 032120 (2012).

[41] Y. Komorida, M. Mito, H. Deguchi, S. Takagi, A. Millán, N. J. O. Silva, and F. Palacio, Appl. Phys. Lett. **94**, 202503 (2009).

[42] P. V. Hendriksen, S. Linderoth and P. A. Lindgard, Phys. Rev. B **48**, 7259 (1993) .

[43] D. T. T. Nguyet, N. P. Duong, L. T. Hung, T. D. Hien, and T. Satoh, J. All. Comp. **509**, 6621 (2011).

[44] K. Mandal, S. Mitra, and P. A. Kumar, Europhys. Lett. **75**, 618 (2006).

[45] J. P. Chen, C. M. Sorensen, K. J. Klabunde, G. C. Hadjipanayis, E. Devlin, and A. Kostikas, Phys. Rev. B **54**, 9288 (1999).

[46] C. R. Alves, R. Aquino, M. H. Sousa, H. R. Rechenberg, G. F. Goya, F. A. Tourinho, and J. Depeyrot, J. Metast. Nanocryst. Mater. **20–21**, 694 (2004).

[47] F. J. Owens, J. Phys. Chem. Solids **64**, 2289 (2003).